

# Orbital ordering and frustration of $p$ -band Mott-insulators

Congjun Wu

Department of Physics, University of California, San Diego, CA 92093

We investigate the general structure of orbital exchange physics in Mott-insulating states of  $p$ -orbital systems in optical lattices. Orbital orders occur in both the triangular and Kagome lattices. In contrast, orbital exchange in the honeycomb lattice is frustrated as described by a novel quantum  $120^\circ$ -model. Its classical ground states are mapped into configurations of the fully-packed loop model with an extra  $U(1)$  rotation degree of freedom. Quantum orbital fluctuations select a six-site plaquette ground state ordering pattern in the semiclassical limit from the “order from disorder” mechanism. This effect arises from the appearance of a zero energy flat-band of orbital excitations.

PACS numbers: 03.75.Ss, 03.75.Nt, 05.50.+q, 73.43.Nq

Orbital is a degree of freedom characterized by orbital degeneracy and orientational anisotropy. The interplay among orbital, spin and charge degrees of freedom gives rise to important effects on metal-insulator transitions, superconductivity, and colossal magneto-resistance in transition metal oxides [1, 2, 3]. The progress of cold atom physics in optical lattices has provide a new opportunity to investigate orbital physics. A major advantage of optical lattices is the absence of the Jahn-Teller lattice distortion which lifts orbital degeneracy and quenches the orbital degree of freedom in solid state systems.

Orbital physics in optical lattices exhibits different features from those in solid state systems [4, 5, 6, 7, 8, 9, 10, 11, 12, 13, 14, 15, 16]. The Hubbard interaction of  $p$ -orbital bosons has the ferro-orbital nature leading to an “orbital Hund’s rule”. This generates a class of orbital superfluid states with complex-valued wavefunctions breaking time reversal symmetry beyond Feynman’s celebrated argument of the positive-definitive ground state wavefunctions [6, 7, 8]. The  $p$ -orbital honeycomb lattice filled with fermions provides a  $p_{x,y}$ -orbital counterpart of graphene, whose flat band structure dramatically enhances interaction effects and gives rise to various charge and bond crystalline orders [11, 17]. The experiment progress is truly exciting [13, 14, 15, 16]. In particular, the meta-stable  $p$ -orbital bosonic systems have been realized by using the stimulated Raman transition to pump bosons into high orbital bands [16].

In Mott-insulators, the orbital degree of freedom also enables super-exchange interaction just as spin does. A marked difference between orbital and spin exchanges is that the former depends on bond orientation. Orbital exchange physics has been extensively investigated in the  $d$ -orbital  $t_{2g}$  and  $e_g$  systems [3, 19, 20, 21, 22]. However, correlation effects in the  $p$ -orbital bands in solid state systems are typically weak. To our knowledge, the  $p$ -orbital exchange physics has not been investigated in solid state systems. In contrast, the  $p$ -orbital systems in optical lattices can be easily tuned to the strong correlation regime, providing an opportunity to investigate new orbital physics. A discussion of the  $p$ -orbital exchange in the honeycomb lattice and the consequential  $120^\circ$  degree

model was presented by the author in Ref. [23].

In this article, we construct the general structure of the  $p$ -orbital exchange models in optical lattices. Orbital orders are found in the square lattice, and also in the triangular and Kagome lattices which are typical frustrated lattices for spin systems. In contrast, strong orbital frustration occurs in the honeycomb lattice as described by a novel  $120^\circ$ -orbital exchange model. The classical ground states are closely related to the fully-packed loop representation of the three-coloring model. The “order from disorder” mechanism generates a plaquette orbital ordering pattern from quantum orbital fluctuations.

We begin with the two dimensional  $p_{x,y}$ -orbital Mott-insulators with spinless fermions by loading a single component of fermion atoms. Each optical site is approximated by an anisotropic harmonic potential well with frequencies  $\omega_z \gg \omega_x = \omega_y$ . Suppose that the filling is two fermions per site: one is in the inert  $s$ -orbital and the rest fills the  $p_{x,y}$ -orbitals. The hopping terms in the  $p$ -bands can be classified as the  $\sigma$ -bonding  $t_{\parallel}$  and  $\pi$ -bonding  $t_{\perp}$  (typically  $t_{\parallel}/t_{\perp} \gg 1$ ). Due to the orbital degeneracy, the on-site interaction for spinless fermions is still the Hubbard-like as  $H_{int} = U \sum_{\vec{r}} n_{\vec{r},x} n_{\vec{r},y}$ . For spinless fermions, the leading contribution to  $U$  is from the  $p$ -wave scattering. In order to enhance  $U$ , we suggest using fermions with large magnetic moments polarized in external magnetic field, such as  $^{53}\text{Cr}$  with  $6\mu_B$ . Another method is to use the  $p$ -wave Feshbach resonance to enhance  $U \gg t_{\parallel}$ . But we do not need very close to the resonance, so that  $U$  is still smaller than the gap between  $s$  and  $p$ -bands to avoid multi-band effect.

The  $p$ -orbital exchange physics can be conveniently represented by using the pseudospin  $\tau$ -vectors defined as  $\tau_1 = \frac{1}{2}(p_x^\dagger p_x - p_y^\dagger p_y)$ ,  $\tau_2 = \frac{1}{2}(p_x^\dagger p_y + h.c.)$ ,  $\tau_3 = \frac{1}{2i}(p_x^\dagger p_y - h.c.)$ , where  $\tau_{1,2}$  describe the preferential occupation of orbital orientation,  $\tau_3$  is the orbital angular momentum. Let us first look at the  $x$ -bond. Since  $p_{x,y}$ -orbitals are eigenstates of  $\tau_1$  with eigenvalues of  $\pm\frac{1}{2}$ , respectively, this exchange is Ising-like in the absence of  $\pi$ -bonding as  $H_{ex}(\vec{r}, \vec{r}') = J_{\parallel} \tau_1(\vec{r}) \tau_1(\vec{r}')$  with  $J_{\parallel} = 2t_{\parallel}^2/U$ . Moreover, the Ising quantization axis changes with bond orientations. For a bond along a general direction of

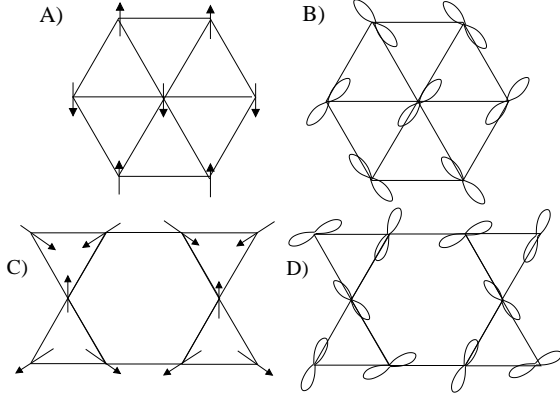


FIG. 1: The  $\tau$ -vector (A and C) and the corresponding orbital (B and D) configurations. The  $p$ -orbitals in the triangular lattices form  $45^\circ$  and  $135^\circ$  angles with the  $x$ -axis, and those in the Kagome lattices are  $15^\circ$ ,  $75^\circ$ , and  $135^\circ$ .

$\hat{e}_\varphi = \cos \varphi \hat{e}_x + \sin \varphi \hat{e}_y$ , we can rotate  $p_{x,y}$ -orbitals at an angle of  $\varphi$ . In the new basis of  $p'_x = \cos \varphi p_x + \sin \varphi p_y$  and  $p'_y = -\sin \varphi p_x + \cos \varphi p_y$  which are the eigenstates of  $\cos 2\varphi \tau_1 + \sin 2\varphi \tau_2$ , the exchange along the bond remains Ising-like as

$$H_{ex}(\vec{r}, \vec{r} + \hat{e}_\varphi) = J_{\parallel} [\vec{\tau}(\vec{r}) \cdot \hat{e}_{2\varphi}] [\vec{\tau}(\vec{r} + \hat{e}_\varphi) \cdot \hat{e}_{2\varphi}]. \quad (1)$$

The exchange model in the lattice is just a summation of Eq. 1 over all the bonds. Although the  $p$ -orbital system is of pseudospin-1/2, we will take the  $\tau$ -operators as general spin- $S$  operators below.

Orbital ordering appears in all of the square, triangular, and Kagome lattices. In the square lattice, Eq. 1 reduces to the 2D Ising-model with the staggered ordering. For the triangular and Kagome lattices depicted in Fig. 1, we rotate  $p$ -orbitals on each site at  $180^\circ$  around the  $x$ -axis which transforms the  $\tau$ -vectors as  $\tau_1 \rightarrow \tau_1$  and  $\tau_{2,3} \rightarrow -\tau_{2,3}$ . Correspondingly, the azimuthal angles  $\varphi_\tau$  of the  $\tau$ -vector and  $\varphi_p$  of the  $p$ -orbitals satisfy  $\varphi_\tau = -2\varphi_p$  ( $\varphi_p$  has a periodicity of  $\pi$  instead of  $2\pi$ ). Then Eq. 1 along each bond changes to  $H_{ex}(\vec{r}, \vec{r} + \hat{e}_\varphi) = J_{\parallel} [\vec{\tau}(\vec{r}) \cdot \hat{e}_\varphi] [\vec{\tau}(\vec{r} + \hat{e}_\varphi) \cdot \hat{e}_\varphi]$  for  $\hat{e}_\varphi = \pm \hat{e}_x, \pm(\frac{1}{2}\hat{e}_x \pm \frac{\sqrt{3}}{2}\hat{e}_y)$ . In the triangular lattice, the exchange model can be re-organized into  $H_{tri} = \frac{J_{\parallel}}{2} \sum_{\vec{r}, i=1 \sim 6} \{ [\vec{\tau}(\vec{r}) + \vec{\tau}(\vec{r} + \hat{e}_{\varphi_i})] \cdot \hat{e}_{\varphi_i} \}^2 + J_{\parallel} \sum_{\vec{r}} [\tau_3^2(\vec{r}) - S(S+1)]$ . Thus the classic ground state configurations satisfy  $\tau_3(\vec{r}) = 0$  on each site and  $[\vec{\tau}(\vec{r}) + \vec{\tau}(\vec{r} + \hat{e}_{\varphi_i})] \cdot \hat{e}_{\varphi_i} = 0$  on each bond. For two neighboring sites  $i$  and  $j$ , their azimuthal angles  $\varphi_i$  and  $\varphi_j$  of  $\tau$ -vectors should satisfy either  $\varphi_j = \varphi_i + \pi$  or  $\varphi_j = 2\varphi(\hat{e}_{ij}) - \varphi_i + \pi$  where  $\varphi(\hat{e}_{ij})$  is the azimuthal bond angle. It is straightforward to prove that the only classic configurations satisfying this constraint is depicted in Fig. 1 A as the stripe configuration with  $\tau$ -vectors aligned along the  $90^\circ$  and  $270^\circ$ -directions up to a 6-fold degeneracy associated the lattice rotation group. The corresponding orbital configuration is shown in Fig. 1 B.

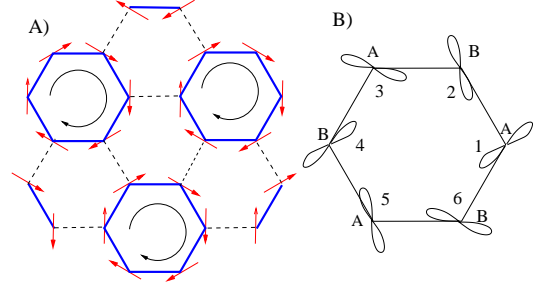


FIG. 2: The fully-packed oriented loop configurations in which  $\tau$ -vectors lie in directions of  $\varphi = \pm 30^\circ, \pm 90^\circ, \pm 150^\circ$ . A) The closest packed loop configuration with all the loops in the same chirality. B) The  $p$ -orbital configuration for one closed loop in A). The azimuthal angles of the  $p$ -orbitals are  $45^\circ, 105^\circ, 165^\circ, 225^\circ, 285^\circ$ , and  $345^\circ$ .

For the Kagome lattice, the classical ground state configurations can be obtained by minimizing the exchange energy for each triangle. It shows that  $\tau$ -vectors lie along the angle bisectors of triangles, which can be consistently arranged over the entire lattice as the “ $Q = 0$ ” state depicted in Fig. 1 C and D. Its ground state is two-fold degenerate by reversing the directions of all of the  $\tau$ -vectors. Their orbital excitation spectra are gapped in both the triangular and Kagome lattices as  $1.68JS$  and  $2.45JS$  within a Holstein-Primakov type orbital wave analysis, respectively

In contrast, the  $p$ -orbital exchange model in the hexagonal lattice is markedly different, which exhibits strong orbital frustrations. Three unit vectors  $\hat{e}_{1,2,3}$  denoting bond orientations are defined as  $\hat{e}_1 = \hat{e}_x$ ,  $\hat{e}_{2,3} = -\frac{1}{2}\hat{e}_x \pm \frac{\sqrt{3}}{2}\hat{e}_y$ . Due to the bipartite nature of the honeycomb lattice, we rotate the  $p_{x,y}$ -orbitals at  $180^\circ$  around the  $x$ -axis in the  $A$ -sublattice and around the in-plane direction of  $\hat{e}_\varphi$  with  $\varphi = 45^\circ$  in the  $B$ -sublattice. This transformation changes the  $\tau$ -operators as  $\tau_1 \rightarrow \tau_1, \tau_{2,3} \rightarrow -\tau_{2,3}$  for the  $A$ -sublattice and  $\tau_{1,3} \rightarrow -\tau_{1,3}, \tau_2 \rightarrow \tau_2$  for the  $B$ -sublattice. The relations between the azimuthal angles of the  $\tau$ -vectors and the  $p$ -orbitals are  $\varphi_\tau = -2\varphi_p$  for the  $A$ -sublattice and  $\varphi_\tau = \pi - 2\varphi_p$  for the  $B$ -sublattice. We arrive at

$$H_{hex} = J_{\parallel} \sum_{\vec{r} \in A, i=1,2,3} ([\vec{\tau}(\vec{r}) - \vec{\tau}(\vec{r} + \hat{e}_i)] \cdot \hat{e}_i)^2 + \frac{3J_{\parallel}}{2} \sum_{\vec{r}} [\tau_3^2(\vec{r}) - S(S+1)]. \quad (2)$$

A similar model is studied for the  $e_{2g}$  orbitals of the transition metal oxides in the 3D cubic lattice [20, 21]. Eq. 2 also has a similar form to the Kitaev model [24]. In contrast, the pseudospin  $\vec{\tau} \cdot \hat{e}_i$  defined here only lies in the  $xy$ -plane.

The classic ground states of Eq. 2 require that all the  $\tau$ -vectors are in plane and every two  $\tau$ -vectors of a bond  $\langle ij \rangle$  have the same projection along the bond direction,

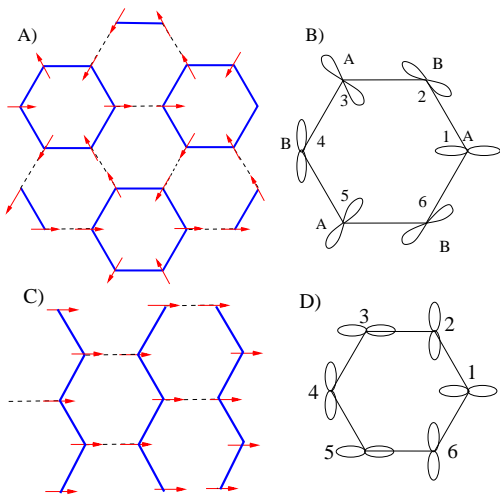


FIG. 3: The fully-packed unoriented loop configurations in which  $\tau$ -vectors lie along the bond directions. A) and C) are the  $\tau$ -vector configurations with the closest packed loops and the ferromagnetic state, respectively. B) and D) are their corresponding  $p$ -orbital configurations.

*i.e.*, the azimuthal angles  $\varphi_i$  and  $\varphi_j$  of the  $\tau$ -vectors satisfy  $\varphi(j) = \varphi(i)$ , or  $\varphi(j) = 2\varphi(\hat{e}_{ij}) - \varphi(i)$ . Clearly the ferromagnetic state with arbitrary in-plane polarization angle satisfies this constraint. In addition, far more other classic ground state configurations can be constructed as follows. Let us pick up an arbitrary lattice site  $i$  and set its  $\tau$ -vector angle  $\varphi_i = 30^\circ$ . Then the angle of the  $\tau$ -vector on any other site can only take one of the values of  $\pm 30^\circ, \pm 90^\circ$ , and  $\pm 150^\circ$ , thus it is perpendicular to one of the three bonds emitted from this site. Let us mark the rest two bonds with bold lines, then those bold lines form loops with the  $\tau$ -vectors lying tangentially to the loops. The ground state configurations are mapped into the fully packed non-intersecting loop configurations in the honeycomb lattice. These loops are oriented in that the chirality of one loop can be changed by flipping the directions of all the  $\tau$ -vectors without affecting other loops. Fig. 2 A shows one of the closest packed loop configurations where each loop goes around the smallest plaquette with the same chirality. The corresponding  $p$ -orbital configuration along the loop is depicted in Fig. 2 B. In the ferromagnetic states with polarization angles of  $\pm 30^\circ, \pm 90^\circ$  and  $\pm 150^\circ$ , all the loops are infinitely long winding around the entire system. Since the allowed loop configurations are numerous, the system is heavily frustrated. It is well-known that this loop representation is equivalent to Baxter's three-coloring model [25, 26, 27]. If all the  $\tau$ -vectors are constrained to take the above six discrete values, these allowed orientations just correspond to the six coloring patterns of each site in the three-coloring model. Since each loop contains even number of bonds, we can assign two colors (e.g.  $R$  and  $G$ ) alternatively to bonds along each loop, and the other

one (e.g.  $B$ ) to bonds normal to each loop. Each loop allows two configurations (e.g.  $RGRG\dots$  and  $GRGR\dots$ ) representing two opposite chiralities.

Next we restore the classic picture of the  $\tau$ -vector as a  $U(1)$  rotor in the  $xy$ -plane. Each loop configuration described above has a global  $U(1)$  degeneracy associated with a suitable arrangement of the clockwise or anti-clockwise rotation of the  $\tau$ -vector on each site. For example, for the configuration depicted in Fig. 2 A, this degeneracy corresponds to a staggered pattern of clockwise and anti-clockwise rotations on  $\tau$ -vectors in two sublattices. For general loop configurations, the rotation directions of two arbitrary neighboring sites are the same or opposite dependent on whether they have the same azimuthal angles or not. For each six-site plaquette with arbitrary  $\tau$ -vector configurations, we have explicitly checked that rotations can be consistently arranged without violating the ground state energy constraint. Since the whole lattice can be decomposed into plaquettes, rotations can also be consistently arranged in the entire system. If we start from one loop configuration and perform a suitable rotation described above at the angles of  $n \times 60^\circ (n = 1 \sim 5)$ , we arrive at other five different oriented loop configurations. As a result, the classical ground state manifold of Eq. 2 is the fully-packed loop configurations multiplied by a global  $U(1)$  rotation with the angle  $-30^\circ \leq \theta \leq 30^\circ$ .

If the rotation angle defined above is right at  $30^\circ$  or other equivalent angles modular  $60^\circ$ , the  $\tau$ -vector on each site is rotated to one of the three bond directions. If we mark the other two bonds with bold lines, they also connect to form loops. For example, after performing the rotation of  $\pm 90^\circ$  at  $A$  ( $B$ ) sites for the loop configuration in Fig. 2 A, we arrive at the configuration in Fig. 3 A. Except a global two-fold degeneracy by flipping the directions of all the  $\tau$ -vectors, these loops are not oriented. The oriented loop configurations with the same loop locations but different chirality distributions can be rotated into the same unoriented loop configuration.

So far we have elaborated the large ground state degeneracy at the classic level, which must be lifted by quantum and thermal fluctuations. For this purpose, we perform a Holstein-Primakov "orbital wave" analysis. We consider the two representative ground state configurations depicted in Fig. 3 A and C, and define that they correspond to the  $\theta = 0^\circ$  state in their continuous manifolds with the parameter of the global rotation angle  $\theta$ . We calculate the  $1/S$ -correction to the ground state energy from the "orbital wave" at arbitrary angles of  $\theta$ . The result is depicted in Fig. 4 and the details will be presented elsewhere. The ground state energies of configurations in both manifolds arrive at the minimum at  $\theta = n \times 60^\circ (n = 0 \sim 5)$ , *i.e.*, the states represented by unoriented loops. Furthermore, the state of Fig. 3 A energetically wins over the ferromagnetic state, and such a state has an important feature: the appearance

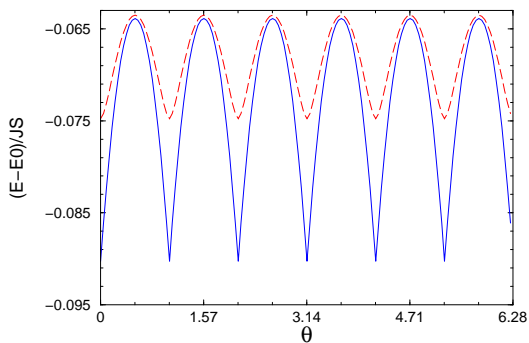


FIG. 4: The “orbital wave” correction to the ground state energy per site for two manifolds of classic ground states depicted in Fig. 3 A (the solid line) and C (the dashed line).  $\theta$  is the rotation angle. The selected ground states correspond to that depicted in Fig. 3 A and its six symmetry related counterparts in which  $\theta = n\frac{\pi}{3}$  ( $\theta = n \times 60^\circ$ ).

of the zero energy flat band of orbital modes. This can be heuristically explained as follows. Let us take an arbitrary six-site loop in this state. Suppose we perform a staggered rotation with a small angle  $\Delta\theta$  only for each site along the chosen loop but without disturbing sites in any other loop. Only the six bonds connecting the chosen loop to outside increase energy. Because the  $\tau$ -vectors in these bonds are along the easy axis, according to Eq. 2, the energy cost vanishes at the quadratic level as

$$\Delta E = 6J_{\parallel}S^2(\Delta\theta)^4. \quad (3)$$

Each unoriented loop contributes one zero energy orbital (at the quadratic level). The state of Fig. 3 A has the maximal number of the zero energy modes. As a result, the quantum zero point motion (orbital fluctuation) selects this state as the true ground state in the large- $S$  limit. We expect that this state not only wins over the ferromagnetic state but also the true ground state in the large- $S$  limit, energetically better than any other configuration which always has less number of zero energy orbital modes. Experimentally, this ordering pattern with the enlarged unit cell of six sites can be easily detected in the time of flight noise correlation spectra. The second-order coherence peaks will appear at the reciprocal lattice vectors of the corresponding reduced Brillouin zone.

Next we briefly discuss the effects from the  $t_{\perp}$  term and finite temperatures. The  $t_{\perp}$  term generates the orbital flipping process as  $\Delta H(\vec{r}, \vec{r}') = J_{\perp} \{ -(\vec{\tau}(\vec{r}) \cdot \hat{e}'_{\vec{r}\vec{r}'})(\vec{\tau}(\vec{r}') \cdot \hat{e}_{\vec{r}\vec{r}'}) + \tau_3(\vec{r})\tau_3(\vec{r}') \}$ , where  $\hat{e}'_{\vec{r}\vec{r}'}$  lies in plane and is perpendicular to  $\hat{e}_{\vec{r}\vec{r}'}$ . For the two ground state configurations depicted in Fig. 3 A and C, this term favors the ferromagnetic state at the classic level by gaining the energy of  $\Delta E_{cl} = J_{\perp}S^2$ , but pays the cost of the zero point fluctuation energy around  $\Delta E_{flc} = 0.01J_{\parallel}S$  as shown in Fig. 4. Due to the smallness of the  $J_{\perp}/J_{\parallel} = t_{\perp}/t_{\parallel}$ ,  $\Delta E_{flc}$  and  $\Delta E_{cl}$  are close to each other and lead to rich phase

competitions. For the realistic system where  $S = \frac{1}{2}$ , the plaquette phase in Fig. 3 c is stabilized roughly at  $t_{\perp} < 0.01t_{\parallel}$  which can be easily realized in the realistic system as calculated in Ref. [17]. On the other hand, thermal fluctuations also help to stabilize the plaquette state which has the maximal number of zero modes by enhancing the entropy contribution.

In summary, we have presented the general structure of the  $p$ -orbital exchange physics, which gives rise to many different features from the  $d$ -orbital solid state systems, including the orbital ordering in triangular and Kagome lattices and orbital frustration of the  $120^\circ$  orbital model in the honeycomb lattice. The six-site plaquette ordering pattern in the honeycomb lattice is found due to the “order from disorder” mechanism. Although the above analysis was done at the large- $S$  level, it is well-known that quantum fluctuations at 2D usually are not strong enough to destroy long range order. It is conceivable that the above orbital orderings also extrapolate to the real orbital systems at  $S = 1/2$ . For example, spin orderings in square and triangular lattices of quantum magnets by large- $S$  methods also apply to the spin-1/2 case.

C. W. thanks C. Nayak, Z. Nussinov for helpful discussions. C. W. is supported by the start up funding at UCSD and Sloan Research fellowship. *Note added* Upon the completion of this manuscript, there appeared an independent work by E. Zhao *et al.* [28] on the orbital exchange model but with different conclusions.

- 
- [1] M. Imada *et al.*, Rev. Mod. Phys. **70**, 1039 (1998).
  - [2] Y. Tokura and N. Nagaosa, Science **288**, 462 (2000).
  - [3] G. Khaliullin, Prog. Theor. Phys. Suppl. **160**, 155 (2005).
  - [4] V. M. Scarola *et al.*, Phys. Rev. Lett. **95**, 033003 (2005).
  - [5] A. Isacsson *et al.*, Phys. Rev. A **72**, 053604 (2005).
  - [6] W. V. Liu and C. Wu, Phys. Rev. A **74**, 13607 (2006).
  - [7] A. B. Kuklov, Phys. Rev. Lett. **97**, 110405 (2006).
  - [8] C. Wu *et al.*, Phys. Rev. Lett. **97**, 190406 (2006).
  - [9] C. Xu *et al.*, Phys. Rev. B **75**, 104428 (2007).
  - [10] C. Xu, arXiv:0706.1609, unpublished.
  - [11] C. Wu *et al.*, Phys. Rev. Lett. **99**, 70401(2007).
  - [12] O. E. Alon *et al.*, Phys. Rev. Lett. **95**, 030405 (2005).
  - [13] A. Browaeys *et al.*, Phys. Rev. A **72**, 053605 (2005).
  - [14] M. Köhl *et al.*, Phys. Rev. Lett. **94**, 80403 (2005).
  - [15] J. Sebby-Strabley *et al.*, Phys. Rev. A **73**, 033605 (2006).
  - [16] T. Mueller *et al.*, Phys. Rev. Lett. **99**, 200405 (2007)
  - [17] C. Wu and S. Das Sarma, arXiv.org:0712.4284, 2007.
  - [18] K. Wu and H. Zhai, arXiv.org:0710.3852, 2007.
  - [19] J. Van den Brink, New Journal of Physics **6**, 201 (2004).
  - [20] M. Biskup *et al.*, Commun. Math. Phys. **255**, 253 (2005).
  - [21] Z. Nussinov *et al.*, Europhys. Lett. **67**, 990 (2004).
  - [22] H. Diep, *Frustrated Spin systems* (World Scientific, 2004).
  - [23] C. Wu *et al.*, cond-mat/0701788v1, 2007.
  - [24] A. Kitaev, Annals of Physics **321**, 2 (2006).
  - [25] J. Kondev *et al.* J. Phys. A **29**, 6489 (1996).
  - [26] J. Kondev *et al.*, Nucl. Phys. B **464**, 540 (1996).
  - [27] R. J. Baxter, J. Math. Phys. **11**, 784 (1970).

[28] E. Zhao and W. V. Liu, arXiv.org:0801.0589, 2008.